Application of in-situ process monitoring to optimize laser parameters during laser powder bed fusion printing of Ti-6Al-4V parts with overhang structures

John Power[1*], Owen Humphreys[1], Mark Hartnett[2], Darragh Egan[1], and Denis P. Dowling[1]

[1]I-Form Centre, School of Mechanical and Materials Engineering, UCD, Belfield, Dublin 4

[2]Irish Manufacturing Research, Block A, Collegeland, Rathcoole, Co. Dublin, D24 WC04

Abstract

Geometrically complex features, such as overhang structures, can be a challenge in laser powder bed fusion (L-PBF), as they can be associated with print defects, such as porosity. In this study, Ti-6Al-4V alloy overhang structures were fabricated using an L-PBF system. Differences were observed in the microstructure in the region around the overhang structures, compared with that observed for the bulk alloy. These included larger grain sizes and a less homogenous microstructure in the print layers closest to overhang structures. It is hypothesized that these microstructural changes are associated with the excess heat generated in the overhang region due to the decreased thermal conductivity of the powder immediately below the print layers, compared with solid alloy. Also observed was an increased level of porosity (up to 0.08%) in the overhang print alloy, compared with the corresponding <0.02% in the alloy bulk. During printing, in-situ process monitoring of the meltpool emissions was obtained in the near-infrared range and correlated with the properties of the printed parts.

This in-process data assisted in selecting optimal laser processing conditions in the first fifteen layers above the overhang to prevent meltpool overheating. By systematically controlling the laser energy during the printing of L-PBF overhang structures, the level of porosity was reduced to match that of the bulk alloy. There was also an associated reduction in the roughness of the overhang itself, with its Ra decreasing from 62.4 ± 7.3 µm to 7.5 ± 1.9 µm.

Keywords: Laser powder bed fusion; Process monitoring; Titanium; Porosity; Roughness

*Corresponding author

1. Introduction

The development of additive manufacturing (AM) technologies, such as laser powder bed fusion (L-PBF), has allowed for the increased flexibility and complexity of designs over formative and subtractive manufacturing processes [1]. L-PBF involves the laser melting of powder particles together using a layer-by-layer approach. It facilitates the production of a range of geometrically complex metallic structures, some with internal micro-scaled architectures. L-PBF fabricated alloy parts are used routinely for applications such as those in the medical device and aeronautical sectors [2, 3]. Part quality is a critical issue for both of these industry sectors; in particular, to avoid issues such as porosity defects, a high level of post-build quality inspection is required [4].

Parameters, such as laser scan speed and beam diameters, have been reported to be important in influencing the formation of porosity in L-PBF printed parts [5, 6]. Three mechanisms have been reported to be associated with the generation of porosity [7]. These are, firstly, gas porosity arising from inert gas entrapment or vapour alloys inside the meltpool. These can lead to the formation of small spherical-sized pores, known as gas pores [8]. Incomplete melting of the powder due to rapid scanning speeds or low power can result in small irregularly shaped pores, referred to as a lack of fusion (LOF) pores. In contrast, excessive laser power or slower scanning speeds can cause keyhole

(KH) pore formation, where the material in the meltpool is vaporized, and this vapour is trapped in the resolidifying alloy, resulting in bubble-like cavities after solidification [5]. This over-melting of the powder bed significantly affects the incorporation of unmelted powder, leading to the formation of voids and porosity.

Another factor that can influence the porosity and morphology of L-PBF printed parts is the heat transfer from the meltpool during part manufacturing [9-13]. Examples of geometric features that affect heat transfer in L-PBF parts include lattice structures [14], support structures [10], and unsupported overhangs [12]. The current investigation evaluates the impact of laser processing conditions on the printing of unsupported overhang structures. It is reported that the roughness (Ra) of L-PBF overhang prints is affected by parameters such as layer thickness and the build angle [15, 16]. At larger layer thickness, the laser scan tracks can become misaligned, caused by an unstable meltpool, which in turn could lead to discontinuities within the melted material, causing surface pores. Increased laser scanning speed and decreased laser power have been shown to correlate with an increase in the roughness of L-PBF parts [17]. At high scanning speeds, the balling of molten powder can occur, which can disrupt the edge of the meltpool and affect the layer's shape [18]. It is reported that one source of increased roughness is due to Raleigh instability; this arises due to the molten pool elongating at high scanning speeds, breaking into small islands [19]. This results from the surface tension gradient-driven flow inside the molten pool, known as Marangoni convection. The principle fluid forces in laser meltpools for laser material processing have been extensively studied and can be summarised as follows: buoyancy force (caused by the spatial variation of the liquid metal density), Marangoni force (caused by surface tension gradients), gravity force and shear force [20]. When evaporation occurs in the keyhole melting mode, however, it is reported that recoil pressure becomes the principal driving force of the molten metal [21]. Figure 1 helps to illustrate the powder melting and solidification evolution process in L-PBF [22]. When the laser is turned on, the beam energy is absorbed by the powder layer and the powder melts, resulting in a depression area, associated with the recoil force, caused by the evaporation of material, Figure 1. As the application of laser beam is in a Gaussian distribution, a temperature gradient is created between the centre and the edges of the meltpool, which induces surface tension and causes the Marangoni effect to occur. Lastly, the depression area is filled with fluid by the Marangoni effect, Figure 1. The result is a curved wave-like solidified track.

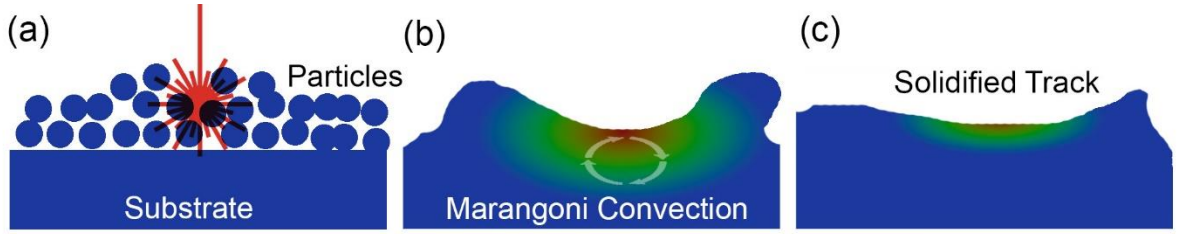

Figure 1: Powder melting and solidification process evolution (a) initial state (b) heating process (c) solidification.

Post-build quality control techniques, particularly micro-computed tomography (µCT), have been used to non-destructively evaluate printing defects such as porosity, along with the enhanced level of roughness around overhang structures [4]. If these printing defects could be identified and corrected during alloy part printing, it would enhance the efficiency of the AM process and reduce process waste.

Amongst the in-process monitoring techniques used to monitor L-PBF printing are optical emission spectroscopy and thermal monitoring [4, 10, 11, 23-25]. Most L-PBF in-process monitoring systems use on-axis photodiodes and high-speed cameras to monitor the optical emissions from the laser

meltpool, along with the meltpool size and shape, respectively. To date, there have been relatively few examples of investigations that correlated in-situ data associated with changes in L-PBF print parameters and the resulting printed part geometries. For example, Alberts et al. [24] demonstrated a correlation between an L-PBF system (SLM 280), infrared photodiode signals and the volumetric energy used to print the part. When the powder layer thickness in the build was decreased, a direct response in the photodiode signal could be seen. Egan et al. [11] compare the accuracy of part dimensional data obtained using in-situ optical emission spectroscopy during L-PBF (Renishaw RenAM 500M) printing with post-build µCT scans of the same parts. It was demonstrated that for 600 µm diameter cavities, the in-process and post-print cavity measurements were within 1.7% of each other. However, the closeness of fit decreased significantly for smaller diameter cavities. This study also highlighted that when the laser is processing the first layer above a cavity, the poor thermal conductivity of the alloy powder, compared to the solid alloy, results in an increased melt pool size and temperature. This increased temperature, arising from a decrease in thermal conduction away from a meltpool generated in an overhang, may result in large thermal gradients, which can, in turn, destabilize the meltpool. A larger thermal gradient may impact both the level of porosity generated and the alloy microstructure of the layers immediately above an overhang [12]. A further example of this effect is a report by Scime et al. [13], who imaged laser meltpools while printing unsupported overhangs using an off-axis camera. Significant morphological changes were observed as the meltpools travelled away from printing non-overhang layers to overhang layers. This change in the morphology of the meltpool was consistent with that of previously observed meltpools which had caused keyhole porosity.

In summary, the higher alloy print roughness associated with overhang structures is due to the unequal heat distribution rates in the powder compared to the solid material, creating large thermal gradients which can destabilize the meltpool and disrupt the shape of the layer edge [26]. Powder particles can also contribute, as when they are not fully melted, when insufficient laser power is used, the partially melted powder material adheres to the surface of the build. The average roughness caused by these un-melted particles is on the same order of magnitude as the powder diameter [27].

The present study is focused on the printing of unsupported overhang structures carried out using a Ti-6Al-4V alloy. This alloy is widely applied in engineering applications due to its combination of good mechanical performance, low density and excellent corrosion resistance [28, 29]. When the alloy is produced by forging, it generally exhibits a lamellar microstructure, which consists of acicular α phase, as well as (α+β) lamellar grains, referred to as "basket weave" [30]. During L-PBF, the rapid solidification of the Ti-6Al-4V alloys followed by subsequent thermal cycling results in a non-equilibrium hierarchical as-fabricated microstructure of epitaxial grown prior β grains, aligned with the build direction [31, 32]. These columnar β grains consist of fine acicular primary alpha (α') martensite variants. Several L-PBF parameters are responsible for the formation of the as-built microstructure. Kaschel et al. [33] demonstrated that increased laser power resulted in wider prior β grains and more prolonged and thinner α' needles. Higher meltpool temperatures caused by higher laser powers may have given way to re-melting previously solidified layers in the build. These higher meltpool temperatures may also have induced localized annealing, promoting epitaxial growth. The mechanical properties of this alloy have been demonstrated to be dependent on its microstructural properties [34]. Grain orientation/structure has an effect on the strength of Ti-6Al-4V alloys, with Columnar α+β structure reported to exhibit a higher ultimate tensile strength, compared with equiaxed α+β structure [35]. The phase content also influences the mechanical properties of Ti-6Al-4V parts, with the martensitic α' structure being particularly important [33, 36].

The objectives of this study are to establish the effect the overheating resulting from the presence of an overhang feature has on the porosity, roughness, and microstructure of the printed Ti-6Al-4V part. To examine the potential of in-process monitoring to select optimal processing parameters for the printing of overhang structures as a processing tool to assist in preventing alloy overheating. Thus, the final objective is to achieve a higher level of homogeneity between the porosity and roughness of the Ti-6Al-4V alloy in the region around the overhang so that it is closer to that obtained for the bulk alloy.

2. Materials and Methods

2.1. Materials and processing parameters

Extra-low interstitial Ti-6Al-4V (Grade 23, ELI-0406) powder with particle size in the range of 10-45 µm was sourced from Renishaw Plc [37]. This powder exhibits a spherical morphology and is reported by the provider to have low thermal expansion and conductivity [37]. This printing study was carried out on a Renishaw RenAM 500M system that operates under an inert gas atmosphere. This equipment has a modulated 500 W pulse wave emission laser, which fires with a wavelength of 1070 nm, and a modulated 10 ms delay between exposures. The laser follows a Gaussian beam profile that is achieved through the use of a dynamic focusing system that uses two galvo mirrors, correcting the near-parabolic focal length change required as the beam travels across the bed, maintaining the beam in focus. Additionally, this AM system has an in-situ processing monitoring (PM) system called InfiniAM Spectral [38]. The latter system uses a number of photodiodes to gather data relating to the thermal and optical emissions from the laser meltpool created during the build process, as well as providing feedback on the laser energy output from the machine [14]. The MeltView module contains two co-axial photodiodes that detect and record the meltpool emissions in the near infra-red and ultra-violet ranges. The LaserView module uses a single photodiode to monitor the laser output energy. The co-axial nature of this PM system results in a field of view that is determined by the laser scanning system. As the data is recorded by the PM system at 100 kHz, it is reconstructed into 2D and 3D representations of the build in real time.

As the objective of this study was to evaluate if in-process monitoring could be used to select optimized process parameters for the printing of overhang structures, the Ti-6Al-4V test sample in this study was designed to simulate a flat overhang structure. Figure 2 shows the design of the test piece used in this study, with the overhang region highlighted by dashed lines in the plan and side view of the drawing schematic. The first overhang layer began printing after 10 mm (464 layers) of powder material had been deposited and melted to form the solid leg structures to the sides of the overhang. The first overhang layer was deposited directly onto the unsolidified powder material below without the aid of part supports. The overhang area of the test piece was 2 mm x 10 mm.

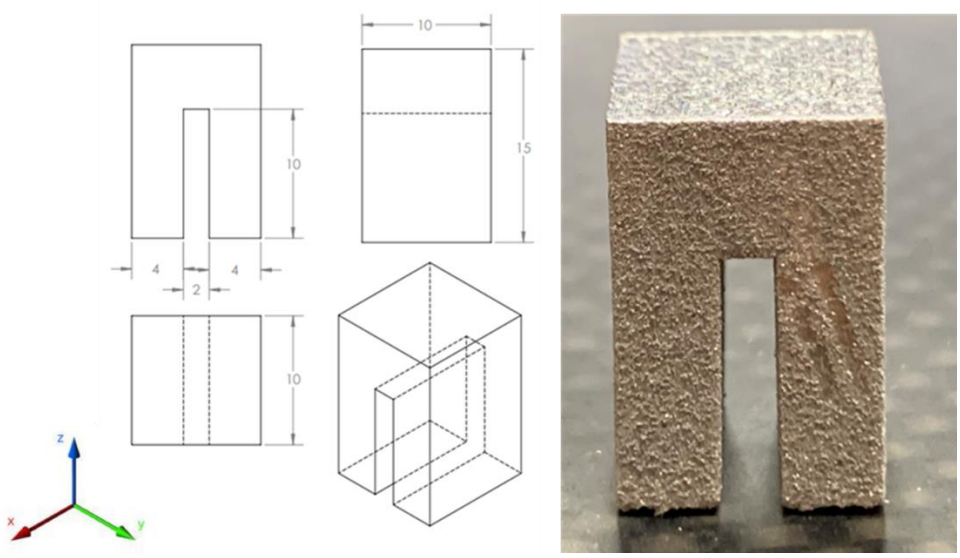

Figure 2: Overhang test piece design and dimensions (in millimetres), along with the printed Ti-6Al-4V alloy part. The print direction is parallel with the z-axis.

The non-overhang regions of each sample's layers of each sample were printed using the laser parameters recommended by the machine's manufacturer for Ti-6Al-4V alloy. The overhang samples were built using pulse laser mode with a 65 µm hatch distance using a meander zig-zag scan strategy, rotated 67^0 degrees between each layer. A spot size of 80 µm, layer thickness of 30 µm and point distance of 75 µm. In the non-overhang regions, a laser power of 200 W and exposure time of 50 µs was used. Additionally, the samples were deposited with the corner of the part facing the recoater blade to minimize the contact area between the fresh powder and the molten alloy. In modulated wave emission, the scan speed between exposure points, s_p (mm/s), can be determined by dividing the point distance (d_p) by the exposure time (e_t) plus the delay between exposures (e_d) as follows:

$$s_p = \frac{d_p}{(e_t + e_d)} \left[\frac{mm}{s}\right]$$

Equation 1: Formula to calculate scanning speed between exposure points.

Using Equation 1, the approximate scan speeds between points was 7.5 mm/s for the non-overhang regions. The delay time between each recoating of the powder was approximately 30 s, and a gas flow rate (Ar) of approximately 29 m^3/h was used during printing.

2.2. Design of experiments study

It is hypothesized that overhang overheating is caused by the mismatch between the laser input energy and the required meltpool temperature to melt but not overheat the Ti-6Al-4V alloy in the region of the overhang. A design of experiments (DOE) was proposed in order to help identify the processing conditions, which would yield a more homogeneous overhang meltpool temperature profile, which would be comparable with that obtained within the bulk alloy. A Box-Behnken design was used to alter three parameters: the laser power and laser exposure time in steps of 5.0%, 12.5%, or 20.0% in either one, eight, or fifteen layers above the overhang. For example, test condition 6 involved a laser power reduced by 5% over eight layers. This thus involved the print of the first overhang layer with 66% of laser power (133W). Each subsequent layer was then printed with an increase of laser power of 5% from the previous layer until the laser power reached nominal laser power (200W). The parameter changes are only applied to melt tracks printed directly onto the 2 x

10 mm overhang region in the centre of the part after layer 464 for either one, eight, or fifteen print layers. This DOE resulted in thirteen print experiments, with three replicates; in all, thirty-nine overhang samples were investigated, as detailed in

Table 1 and Figure 3. The volumetric energy density (VED) for each sample was calculated using Equation 2 [39].

$$VED = \frac{P\, e_t}{h\, d_p\, d_h} \left[\frac{J}{mm^3}\right]$$

Equation 2: Volumetric energy density formula for parts printed using modulated wave laser [39].

Where P (W) is the laser power, e_t (µs) is the laser exposure time, h (µm) is the layer thickness, d_p (µm) is the point distance, and d_h (µm) is the hatching distance. The VED for the non-overhang regions of the build was calculated as 68.4 J/mm^3.

Table 1 contains the average VED for the overhang region over fifteen layers above the overhang.

Table 1: The design of experiments processing conditions investigated. Detailed is the percentage reduction in laser power, along with the exposure time reduction, which indicates the percentage change between subsequent layers until parameters are returned to nominal levels. Also included are the number of layers for which the laser processing parameters were reduced. The final column provides an indication of the overall level of laser energy reduction.

Test Condition	Power Reduction (%)	Exposure Time Reduction (%)	No. of gradient layers	Average VED deposited into the 15 layers above overhang (J/mm^3)
1	12.5	5	1	67.6
2	5	12.5	1	67.6
3	5	20	1	67.3
4	20	5	1	67.3
5	20	20	1	66.7
6	20	20	8	39.8
7	5	5	8	55.5
8	12.5	12.5	8	45.0
9	20	5	15	14.2
10	12.5	20	15	10.6
11	5	5	15	33.1
12	20	12.5	15	10.6
13	5	20	15	14.2

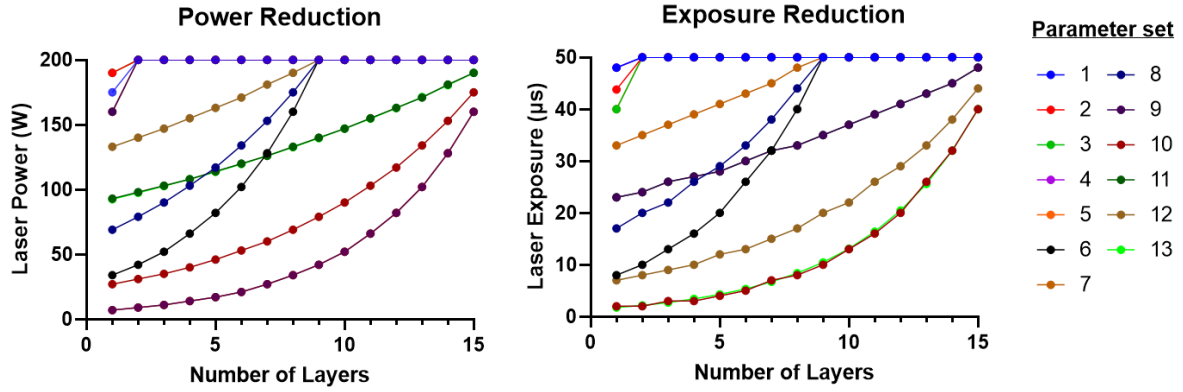

Figure 3: The laser power and exposure time settings for the fifteen layers printed above the overhang. As illustrated, the DOE examines the effect of reducing the laser energy by different magnitudes and the effect of ramping up the laser energy back to the nominal value used within the bulk alloy, using the different laser energy levels shown.

To evaluate the success of the DOE, meltpool emissions in the overhang regions were compared with those in the non-overhang regions in the same print layer. This was done by comparing the in-process monitoring IR (MeltView) photodiode readings. The MeltView photodiode intensity reading of the build was calculated using reconstructed 2D views of each print layer. The pixel intensity associated with each part seen in PM software was obtained by taking images of the 2D reconstructions of each layer and analyzing them using ImageJ software. This allowed for quantifiable values relating to the intensity of the meltpool monitoring photodiodes to be obtained. Additionally, melt tracks printed directly onto the overhang could be isolated in the image analysis, and their photodiode measurements could then be directly taken and compared to melt tracks printed in non-overhang regions. This analysis of the IR emission data allowed for samples that had not experienced overheating at the overhang to be identified. The roughness and porosity of the two regions were compared to determine if the in-situ data could be used to identify optimized processes.

2.3. Porosity and Roughness Measurements

Part porosity was evaluated using a GE Phoenix Nanotom M microcomputed tomography (µCT) system, operating at 150 kV and 200 µm, with a scan time of approximately 10 minutes [40]. The resolution of each scan was 12 µm, defined as the smallest detectable pore size in the sample. The µCT scans were analyzed using the porosity/inclusion analysis (PLA) module in VGStudio Max version 3.5 [41]. The surface determination tool allows the program to identify the material/air boundary by measuring the grey values of individual 'voxels' or 3D pixels. The PLA module examines the grey value of each voxel within the 3D model to check if it is part of a pore/void, and a group of related voxels is allocated to part of the same pore. VGStudio was used to calculate the total percentage of porosity of one sample from each parameter set. Optical microscopy (OM) was also carried out using an Olympus GX51 optical microscope at 10x magnification. The size and shape of pores at the overhang surface were analyzed to determine the type of porosity present. Porosity was evaluated in the solidified alloy directly above the overhang and in the entire structure to compare the effect the overhang had on porosity formation.

Overhang roughness measurements were obtained based on the µCT measurements using an approach previously applied to AM-printed porous structures [42]. Roughness measurements taken using this methodology were reported to exhibit a strong correlation with the measurements taken using optical profilometry for surfaces with high roughness [42]. The roughness of the overhanging edge was determined based on the profile lines taken from 2D cross-sectional images of the overhang. The overhang profile line was extracted using an ImageJ script written by the first author. This script analyses the pixels along the overhanging edge within a user-selected region of interest and measures the edge roughness in correspondence with ISO 21920-2:2021. The average roughness (Ra), along with the total height of the roughness profile (Rt) parameters, were determined for each test sample using Equation 3 and Equation 4. Ra roughness is the most commonly used metric; however, it is insufficient as a single measurement [43]. For this reason, the Rt roughness was also measured and recorded as it is a better metric for detecting large outliers along a surface profile, and it can be compared with Ra values to determine if the sample's roughness measurements are being influenced by a single feature on the profile [44]. Five measurements were taken from five different cross-sections of each sample.

$$R_a = \frac{1}{l_e}\int_0^{l_e}[z(x)]dx$$

Equation 3: The arithmetic mean of the absolute values of the ordinate values.

$$R_t = \max\big(z(x)\big) - \min\,(z(x))$$

Equation 4: Total height parameter, the sum of the largest height and the largest depth.

2.4. Microstructural Analysis

The as-printed Ti-6Al-4V parts were prepared by grinding using 320 SiC grit paper and polishing using a 9 µm diamond suspension, followed by a 0.04 µm colloidal silica solution with 10% H_2O_2 at 15% concentration, allowing for chemical-mechanical polishing as recommend by Struers Ltd. [45]. Alloy etching was carried out using Kroll's solution (5 ml HNO_3, 10 ml HF (48%), 85 ml distilled water). Optical microscopy was carried out using an Olympus GX51 (Olympus-IMS) optical microscope at 10x magnification.

Electron Back Scattered Diffraction (EBSD) data was obtained for a single alloy sample, which had been prepared using the grinding and polishing methodology described above. Two scans of the sample were made, one in the overhang region of the sample's cross-section and another in the non-overhang region of the same sample. Each sample used an observation window of 250 x 250 µm, and from this analysis, the grain sizes and the relative orientations of the grains in the observation windows were measured. A Field Emission Scanning Electron Microscope (FE-SEM, Tescan Mira3) was used to perform the EBSD analysis. For the EBSD measurements, the samples were tilted at 70° to collect the diffracted electrons emitted from the crystal lattices and to record these diffraction patterns through the EBSD detector (Symmetry Detector, Oxford Instruments). A step size of 0.5 µm was used for each EBSD scan. All the EBSD scanned datasets were post-processed using Oxford Instruments AZtecCrystal software for further quantitative microstructural analysis, such as grain misorientation distributions, grain size statistics and phase analysis.

3. Results and Discussion

The objective of this study was to minimize the meltpool overheating in the region immediately above the print overhang structure in order to minimize the level of porosity and roughness obtained in this region. In order to achieve this objective, a design of experiments (DOE) was carried out in which the level of laser energy was systematically varied for up to 15 layers above the overhang. The impact of this was evaluated based on a comparison of the in-process meltpool data with the porosity and microstructural analysis results obtained from the printed alloy.

3.1. Effect of overhang structures on the microstructural formation and printability of Ti-6Al-4V alloy samples.

When printing overhang structures, L-PBF equipment manufacturers typically recommend print parameters that reduce the laser energy in the region immediately above the overhang. For this reason, an initial investigation was carried out on a Ti-6Al-4V overhang sample, for which the laser power used to print the overhang melt tracks in the first overhang layer was reduced to 10% of nominal levels, which was achieved by reducing the laser power by 90%. The resulting alloy microstructure, which was formed in the overhang layers, was examined and then compared with the alloy structure obtained within the rest of the print using OM and EBSD analysis.

OM analysis of the resulting cross-section of the sample revealed the formation of lamellar microstructures with finer α' grains and limited β grains in the α phase boundaries in the majority of

the sample's cross-section (Figure 4). It was found that for all samples, thin-needle-like structures characteristic of the α' phase were randomly scattered throughout the build [33, 36, 46]. Examination of the non-overhang regions of the build exhibited a greater prevalence of columnar grains, which were found to grow epitaxially during the build. The direction of these columnar grains was in the z-direction towards the build plate. This microstructure is typical of that obtained for L-PBF-printed Ti-6Al-4V alloy parts [33]. Within the remainder of the alloy cross-section closer to the overhang edge, small non-columnar α' colonies formed. The size of these α' colonies varied from 17.9 ± 6.7µm to 28.9±10.2µm in width, with the average size being 25.1 ± 8.9µm. The α' colonies were found within 100 µm of the overhang edge. OM imaging (Figure 4) of the samples showed that the α' needles were shorter and narrower in the overhang region of the samples, which were printed using lower laser energy. Previous research has established a link between shorter α' needle morphology and lower laser power [47].

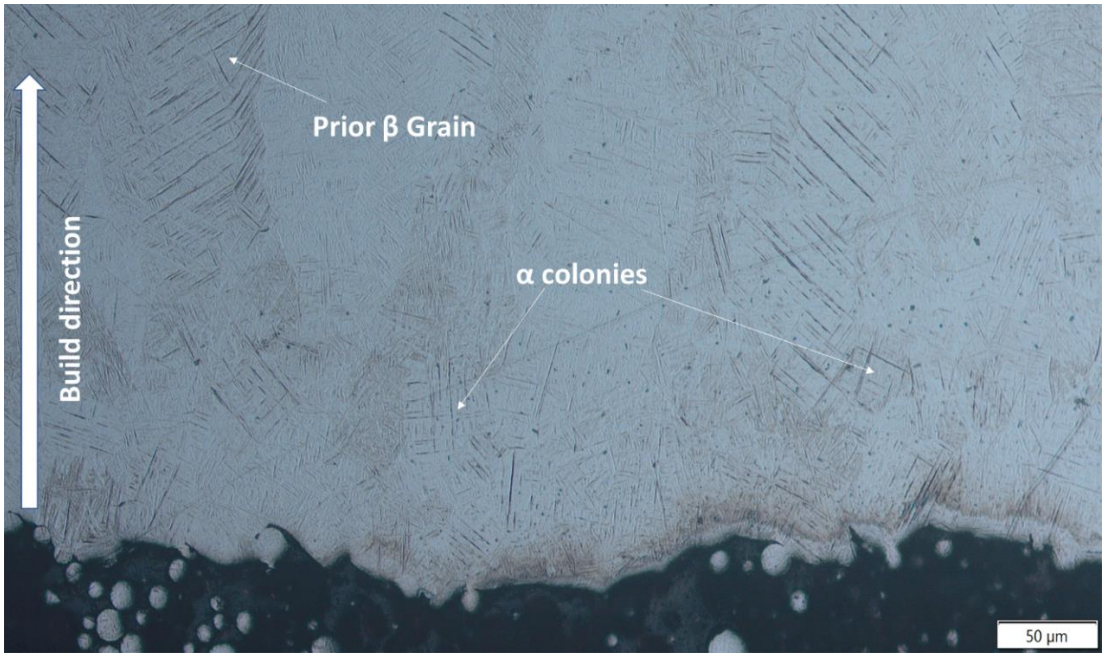

Figure 4: OM image of overhang sample at 10x magnification. The formation of α' colonies dominates the layers printed above the overhang.

EBSD analysis was used to help compare the microstructure in the bulk alloy with that of the region directly above the overhang. Figure 5, obtained from the non-overhang region, shows the formation of a homogenous lamellar microstructure with an average grain size of 7.0 μm^2 and max grain size of 116 μm^2. The grain orientation for both the alpha and beta phases is also relatively homogenous. In contrast, the overhang region microstructure, Figure 5, was found to be less homogenous with an average grain size of 8.7 μm^2 with a max grain size of 309 μm^2 and more randomly orientated crystals. The presence of large grains in the overhang region may have occurred due to grain-coarsening associated with excess heat during laser processing of the alloy powder region [48]. Higher temperatures and slower cooling rates have also been linked to the formation of more randomly orientated crystal grains. These EBSD observations are also supported by the findings obtained from the microscopic analysis of the same samples.

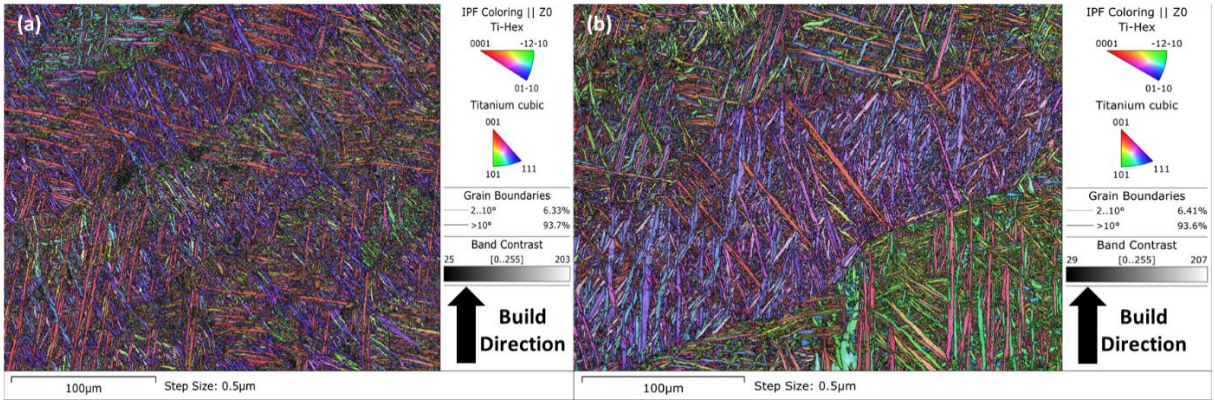

Figure 5: Orientation map for (a) non-overhang region and (b) overhang region of the sample. Both images are taken from a sample using parameter set 2 settings.

As illustrated in Figure 6, cross-section magnification microscopy of the overhang demonstrated the presence of some alloy cracking within the print layers. The cracks observed in the overhang region were most likely thermally induced. A thermal crack can be defined as a crack formed by thermal stresses in the solid state. For brittle intermetallic materials, like Ti-6Al-4V alloys processed via L-PBF, thermal cracking typically occurs at temperatures below the ductile-brittle transition temperature and exhibits cleavage-type fracture [49]. The excess heat observed at the overhang region due to the poor thermal conductivity of the powder material beneath would result in a higher temperature gradient, which in turn increases the thermal stresses in the solidified material. Reducing the thermal gradients in the samples by altering the laser parameters should reduce the thermal stresses in the alloy and prevent cracking.

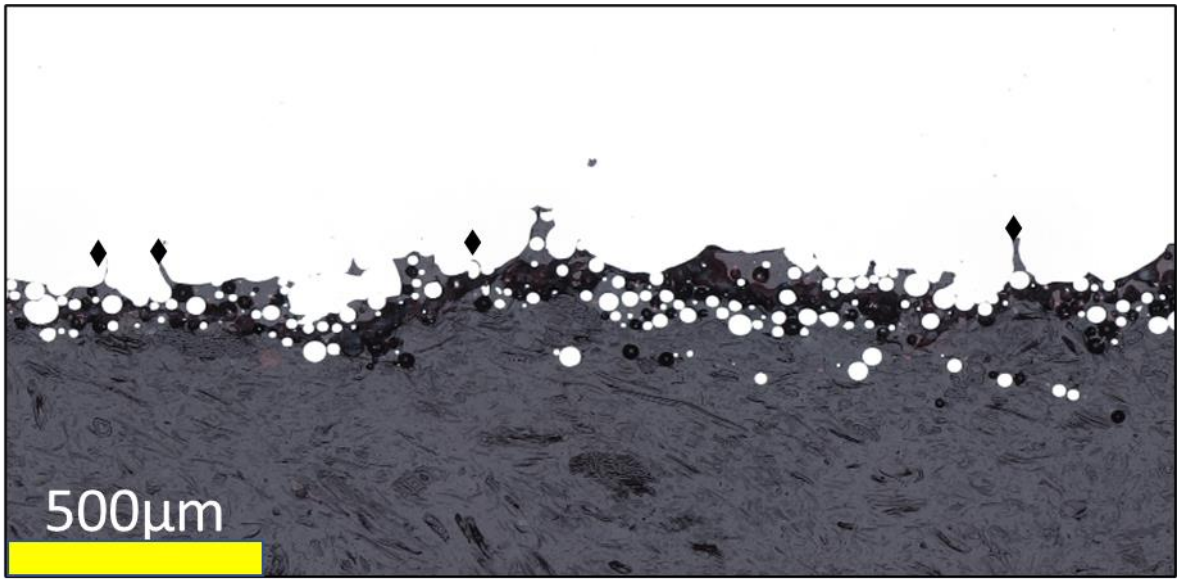

Figure 6: Cross-section of overhang, demonstrating the relatively high surface roughness and the presence of cracking, indicated by the black diamonds.

In-process monitoring of the meltpool for a sample printed using manufacturers' recommendations was carried out using photodiode measurements, as illustrated in Figure 7. The slicing software recommended using 10% nominal laser power, i.e. 20W, for the first three overhang print layers. Despite the reduction in the laser input power to 10% of the nominal power used for the first three print layers, overheating of the meltpool was still found to occur. The meltpool infra-red (IR) emissions were observed to peak between print layers 465 to 467, i.e. within the first three layers

after the power was increased, thus demonstrating the higher meltpool temperatures in this region above the overhang, compared with that obtained in the bulk part. The result in Figure 7 highlights that the manufacturer's recommendation for processing flat overhang structures has still led to overheating of the part in the print layers immediately after the overhang. The remainder of this study was focused on optimizing the laser process parameters to reduce the overheating measured by IR emissions and thus improve the quality of the printed overhang by reducing the measured porosity and roughness in the overhang region.

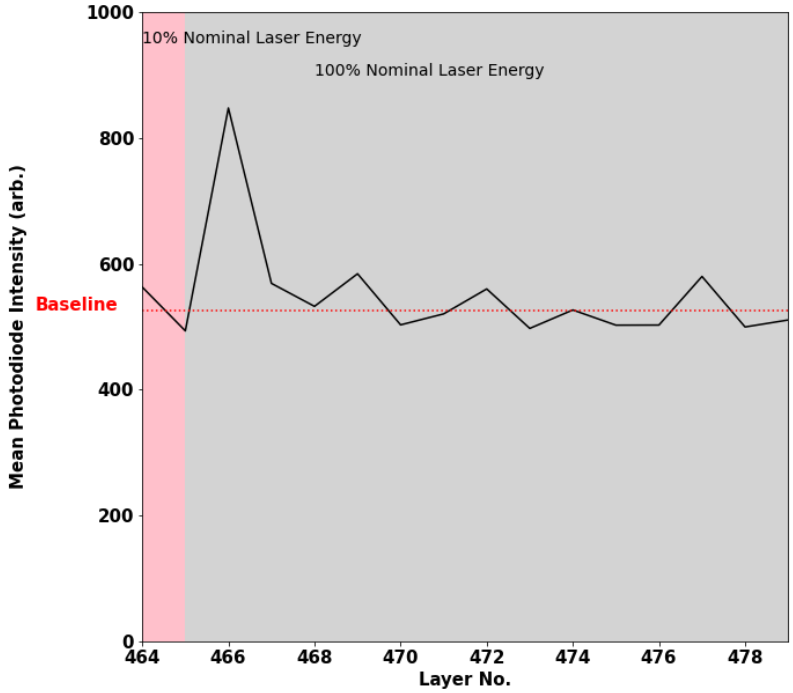

Figure 7: Photodiode emissions obtained from meltpool (arbitrary units) measured using an in-situ IR sensor. A significant increase in the overhang meltpool emissions is detected after the laser power is returned to 100% nominal power. The overhang starts at layer 464.

3.2. Evaluation of DOE results

This evaluation was based on examining the type and level of porosity of the area around the overhang structure and measuring the roughness of the overhang itself. In both cases, the objective was to identify processing conditions that minimized the measured porosity and roughness. The overhang samples were cross-sectioned, mounted, ground, polished and examined using optical microscopy and the type of porosity observed is shown in Figure 8 for a sample printed with low laser energy, demonstrating the presence of LOF porosity. Large irregular pores with sharp corners and edges developed due to the insufficient fusion of metal powder [50]. LOF pores were most evident in printed samples with the largest reduction in VED, samples 6, 9, 10, 12, and 13. A lower energy density value gave rise to incomplete binding between powder particles and layers, resulting in LOF porosity. This result highlights that simply reducing the level of laser energy used to print the overhang can result in different defects than what was observed when excess energy was used.

Figure 8: Lack of Fusion porosity evident in an overhang structure (test condition 13) printed with low laser energy.

Keyhole pores formed in the layers closer to the powder bed in each sample. The poor thermal conductance of the powder bed below the overhang and the initial layers deposited onto the powder bed to form the overhang would have led to an increase in the local meltpool temperature, increasing the chance of material vaporisation and keyhole formation. Keyhole porosity was the most common type of porosity observed in samples printed with a higher laser energy.

Increased porosity was observed in the print layers immediately above the overhang, up to 0.08% volume fraction. This was substantially higher than the level of porosity observed in the bulk alloy regions, which averaged less than 0.02% for all samples. Samples printed with lower laser energy density (test conditions 6, 9, 10, 12, and 13) exhibited higher levels of porosity. This higher porosity level was attributed to two factors. Firstly, the lower laser energy treatments were more likely to generate LOF pores, which are typically larger in size than other types of porosity [51]. Secondly, in addition to the relatively high level of porosity formed immediately above the overhang, additional porosity was also observed at the same print layer height in the 'leg' region, immediately on either side of the overhang. Figure 9 helps to illustrate this, showing the porosity which also formed in the bulk regions at the same level as the overhang. It was concluded that this porosity, which was not observed elsewhere in the sample, was most likely caused by spatter ejection from the 'unstable' overhang meltpool [52].

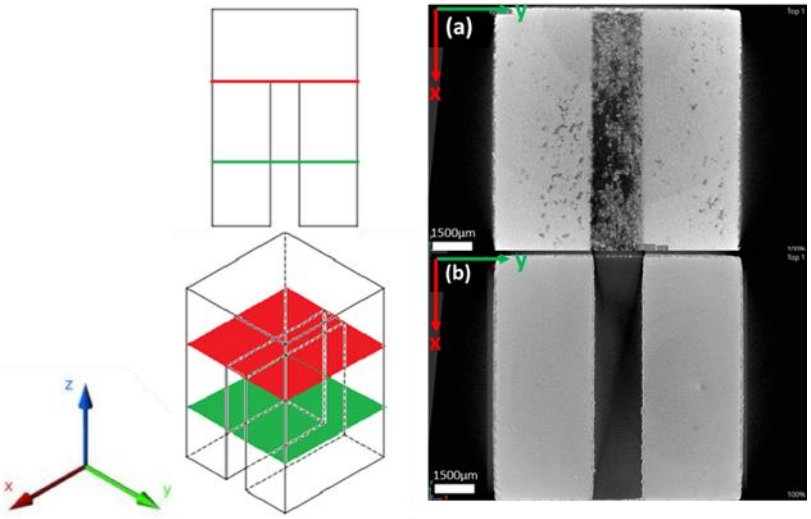

Figure 9: (Left) Schematic showing the plan and isometric view of the overhang test piece. The colour lines and sections indicate the location of the layers: red for layer 464 and green for layer 250. Increased porosity is present in the legs of the

part at the same print level as that of the overhang print layers. (Right) (a) µCT scan images showing the first overhang print layer (layer 464) with increased porosity visible in the non-overhang regions of the part. (b) µCT scan showing print layer (layer 250) with no overhang and no visible porosity.

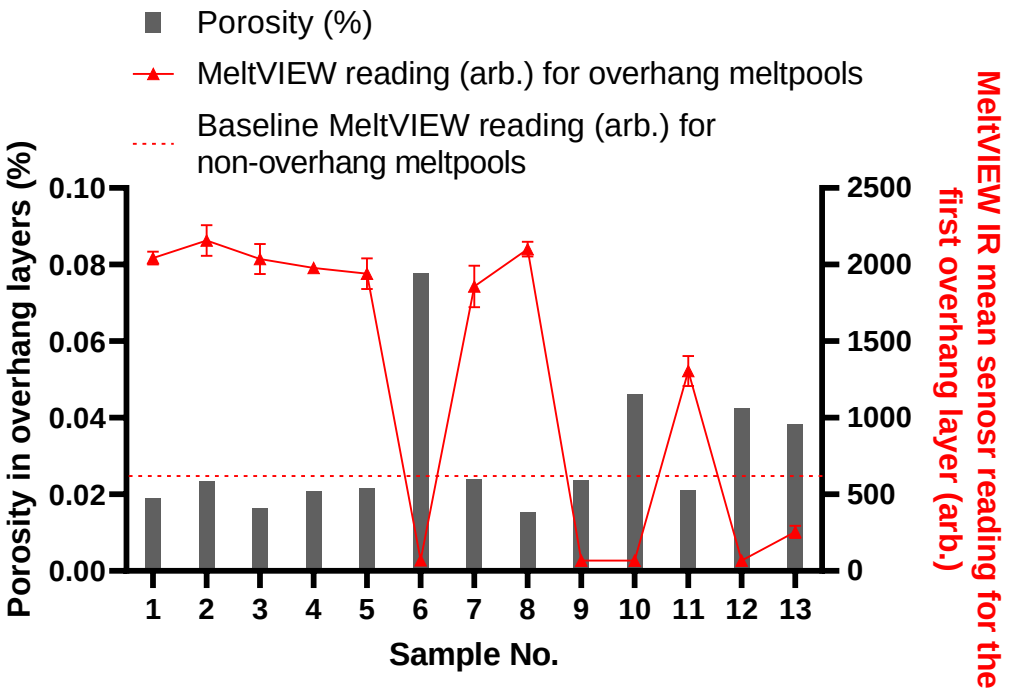

Figure 10 shows the total percentage porosity of the samples as determined using µCT analysis. Also included are the associated in-process photodiode (MeltView) sensor data obtained for the first overhang layer. A trend was observed between the porosity measurements and the recorded MeltView sensor readings. Samples that recorded a lower photodiode signal reading were generally found to exhibit higher levels of porosity. This result was found to also correlate with the cross-sectional microscopy examination, which, based on visual examination, indicated that samples printed with lower laser energies were generally observed to exhibit a higher level of porosity. Sample 8 does not follow this trend, highlighting that while the MeltView sensor reading provides an indication of the level of porosity in a sample, it is not an absolute measurement.

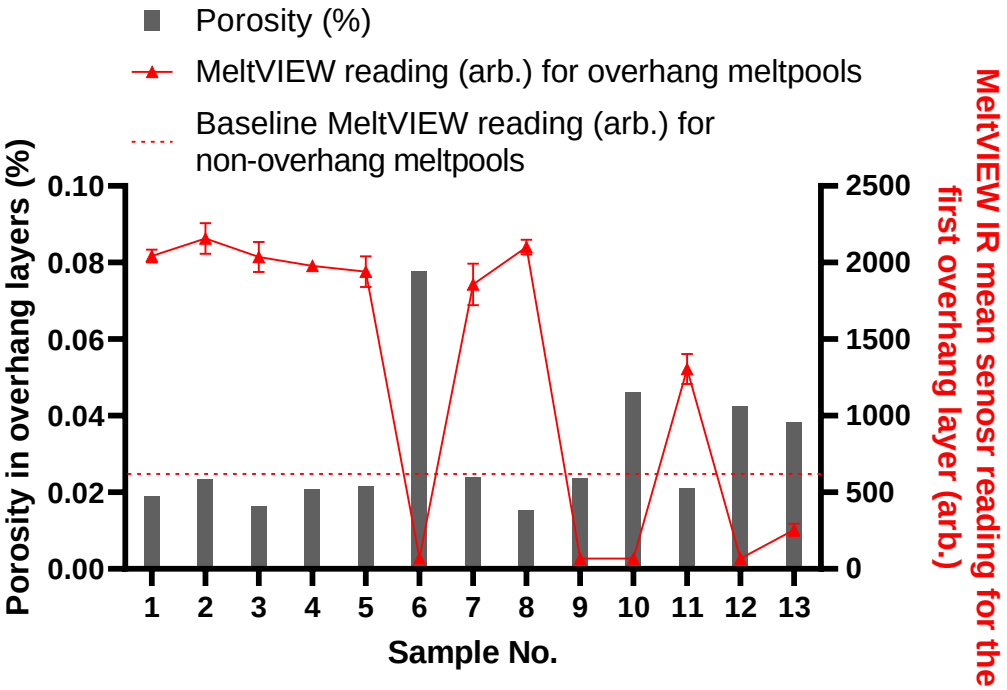

Figure 10: Total porosity (%) of overhang sample measured using µCT data, compared with the mean MeltView IR sensor reading (arbitrary units) obtained from the first overhang layer. Porosity measurements include both keyhole and lack of fusion porosity.

Based on an examination of the cross-sections of the overhang regions, it was concluded that parts printed with higher laser power exhibited fewer unmelted powder particles and a surface with more jagged features and indents. Figure 11 (a) shows an image of a section of an overhang printed with high laser energy (test condition 1). The parameter set used to print this sample was close to the values used for the bulk alloy print. Figure 11 (b) shows the profile plot, measured along the 10 mm length of the overhang, of the same sample printed with high laser energy levels. The large deviations observed in the profile plot can be matched with the significant indents observed in the microscopy images of the corresponding overhang cross-sections. These large individual defects can significantly impact the roughness values obtained. For example, test condition one was found to have the most significant standard deviation in its measured Ra and Rt roughness, with values of 37 ± 28µm and 577 ± 327µm, respectively. In contrast, test condition 13 exhibited the lowest value with Ra and Rt roughness, with values of 8 ± 2µm and 161 ± 32µm, respectively.

A possible explanation for the higher roughness obtained at higher laser powers could be due to the impact of the Marangoni effect, as described in the introduction section (see Figure 1). This may be associated with the formation of an indented profile along the overhang surface, as illustrated in Figure 11 (a). Arising from the relatively high laser energy used and the poor thermal conductivity of the powder material below the overhang, an unequal heat distribution may have been created in the meltpools and as a result of the meltpools being distorted by uneven thermal distribution, a pattern of indents was created.

The microscopy image given in Figure 11 (c) was obtained from an alloy sample printed with low laser energy (test condition 6). It is clear from this image that some of the powder particles located at the overhang layers did not fully melt. As a result, spherical powder particles are observed partially adhering to the overhang. These unmelted particles would contribute to a higher roughness, as described previously by DebRoy et al. [27]. However, these unmelted particles have a

less significant effect on the roughness compared with the more prominent features obtained with higher laser energies. The profile plot of this sample, Figure 11 (d), shows that the roughness of the profile varied considerably along the overhang edge but that the magnitude of this variation was smaller compared to samples printed with higher laser energy.

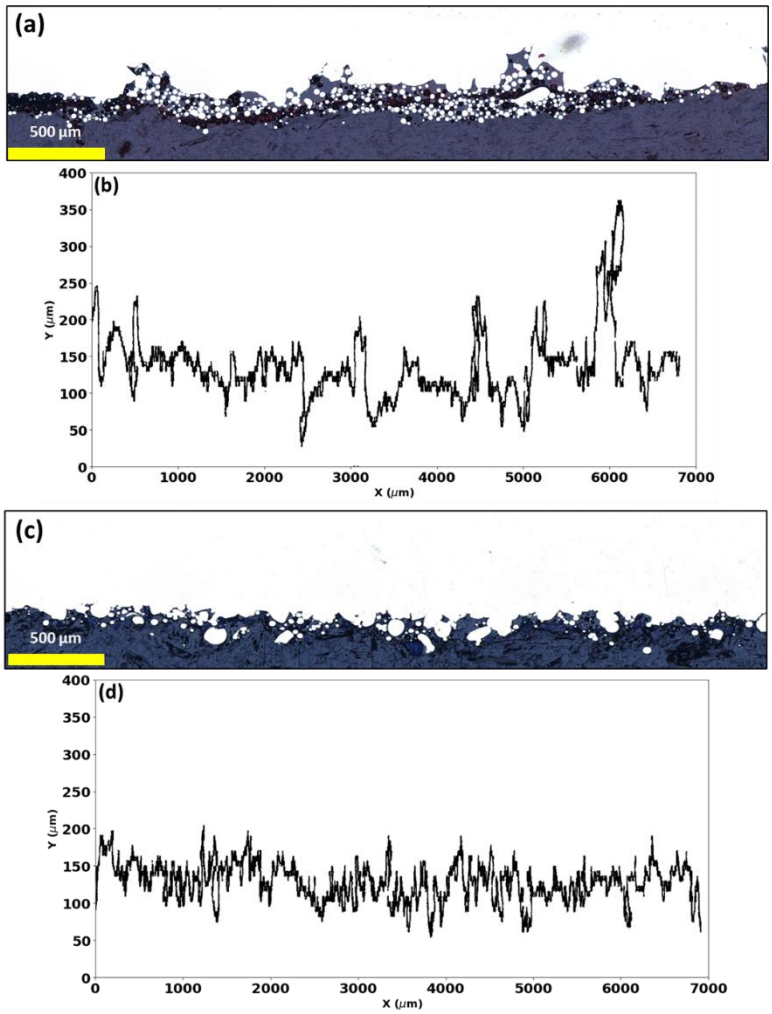

Figure 11: The cross-sectional microscopy images (a) and (c) were obtained for overhangs printed using high (test condition 1) and low (test condition 10) laser energy, respectively. Images (b) and (d) show the corresponding profile plots, measured over the 10 mm length of the overhang, obtained using ImageJ software of the overhang samples cross-sections. Note from the line profiles presented in b and d that the parts printed with the higher laser energy exhibit both a larger variation in y (pixels) along with what visually appears, which indicates a more periodic indent / non-indent profile.

In order to obtain a more quantitative evaluation of the influence of laser energy on overhang roughness (Ra), these two parameters were plotted as illustrated in Figure 12. This demonstrated a positive trend between the intensity of the laser energy used to print the sample and the roughness (Ra) measurements obtained from the µCT scans. This figure also includes the associated photodiode measurements (MeltView data). When higher photodiode measurements were recorded, associated with higher meltpool energy, there was generally an associated increase in roughness. However, this correlation was not observed for all overhang samples, e.g. sample 8. A reduction in laser power, and therefore meltpool temperature, has previously been linked to reduced surface roughness [53]. It was observed that there was a relatively poor correlation between the photodiode data (MeltVIEW) and the Rt roughness. This roughness parameter measures the largest difference between a surface profile's highest peak and lowest valley, and a

factor influencing this poor correlation is that a single surface feature can significantly affect the Rt value of a surface profile.

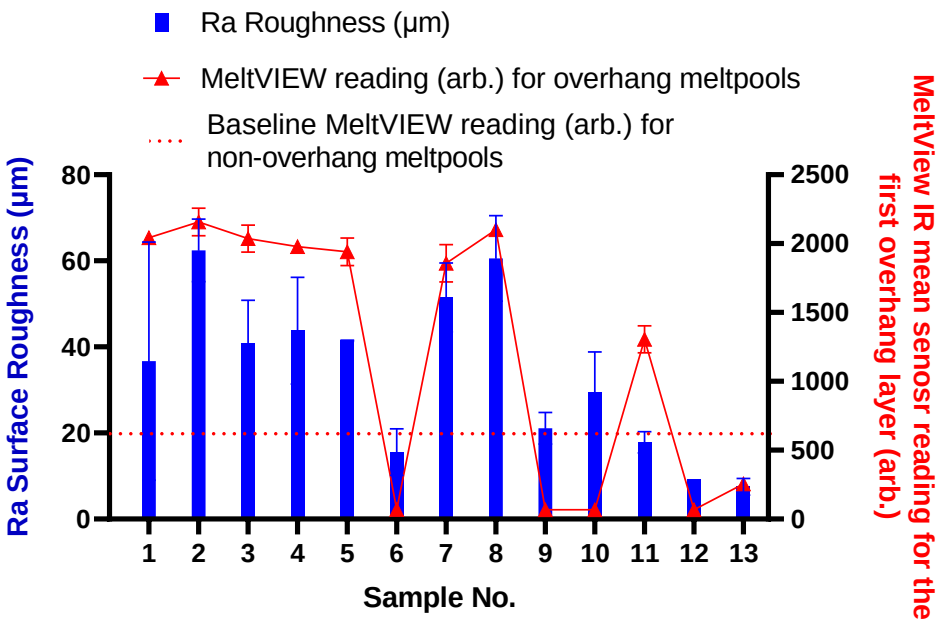

Figure 12: Ra roughness of overhang surface graphed with the average MeltView IR sensor reading (arb.) for the first overhang layer meltpool.

Based on the results from this DOE, the parameters from test condition 11 produced overhang structures with low porosity, 0.02%, and relatively low Ra roughness, 17.8 µm, as well as forming a relatively homogenous overhang morphology. For this print condition, the overhang layers were printed using reduced laser power and exposure time over fifteen layers. The power and exposure time were ramped back up to nominal levels by increasing the laser parameters by 5% over the previous layer's settings. The laser processing conditions were such that energy required to fully melt but not overheat the alloy powder was provided, thus preventing the generation of high levels of porosity.

3.3. In-situ monitoring data

The in-situ photodiode data obtained using the InfiniAM Spectral system during Ti-6Al-4V alloy printing was analyzed to assess if the variation in laser print parameters affected the meltpool energy. It has previously been demonstrated that there is a close correlation between the laser output energy and the InfiniAM photodiode intensity [14]. The current study evaluated the magnitude of meltpool underheating or overheating by comparing the photodiode intensity between the overhang (layer 464) and that obtained in the bulk alloy in layer 450. For almost all the conditions examined in this DOE, the difference between the photodiode intensity and the average (nominal) intensity decreased after the initial overhang layers were printed (Figure 13a). It was therefore concluded that the photodiode intensity variation, particularly in the first three layers above the meltpool, is more relevant to monitoring the meltpool temperature than the average intensity for the non-overhang region. Figure 13 (b) shows the plot of photodiode intensity obtained for a sample printed using test condition 11, which, as highlighted earlier, exhibited both relatively low overhang roughness and porosity. Note the absence of the large photodiode peak, compared with that obtained for an overhang printed with higher laser power (Figure 13 (a)). The sample produced using parameter set 11 had relatively low porosity, 2.1% volume fraction, compared to

other samples. While samples produced using parameters 12 and 13 exhibited lower roughness, there was an increased amount of LOF pores and partially melted and unmelted powder, which reduced the dimensional accuracy of the overhang structure printed under these test conditions. This result shows that optimal process parameters for complex geometries can be selected from a DOE by examining the process monitoring data gathered during the fabrication of the part. An optimal process signature can be identified and then used to select optimal process conditions.

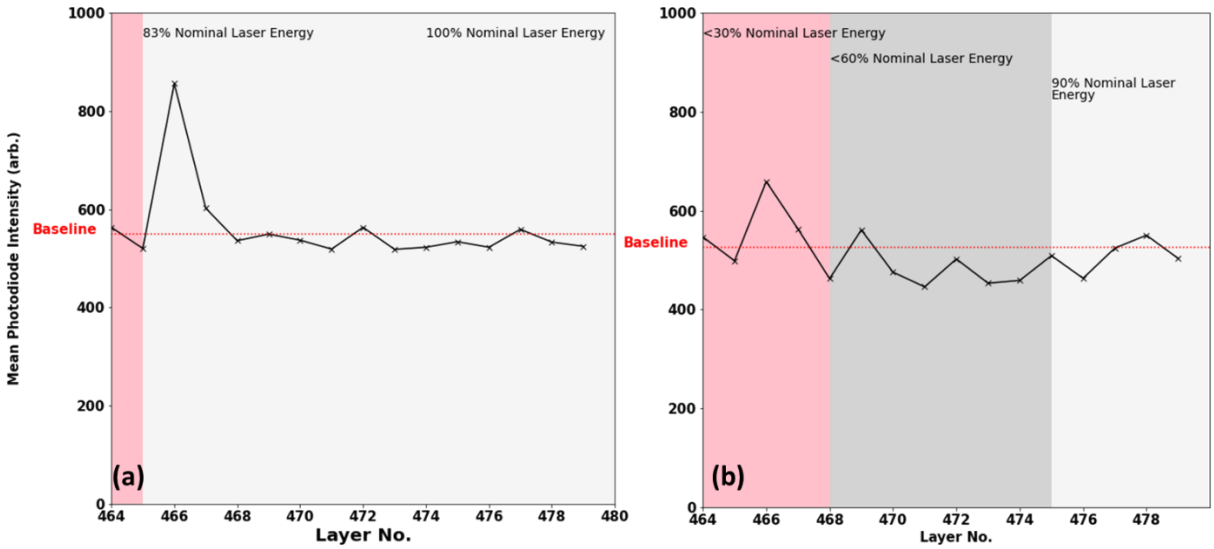

Figure 13: In-situ photodiode (MeltView) sensor readings (arb.) obtained for the first 15 layers over the overhang. The parts were printed using (a) high laser energy (Test condition 1) and (b) low laser energy (Test condition 11) using parameter settings that gradually increased laser power and exposure time from 47% of nominal levels to back to 100% of nominal levels by increasing the levels by 5% from the values of the previous layer over fifteen layers from the first overhang layer. Note the mean photodiode intensity obtained in the non-overhang region is represented by the solid pink line.

4. Conclusions

This study investigated the effect an overhang structure has on the resulting part microstructure, porosity and roughness of Ti-6Al-4V alloy parts produced using LPBF. Additionally, the effect of systematically alternating laser energy on the porosity and roughness was investigated via the use of in-situ process monitoring photodiodes. This study demonstrates the ability of a production-scale L-PBF process monitoring system to identify the optimal printing parameter for parts with complex geometries. Parts printed with optimised laser parameters showed a reduction in porosity and roughness in the layers near the overhang feature. The following conclusions were made from this study:

- EBSD and optical microscopy analysis of Ti-6Al-4V alloy overhang structures showed increased levels of porosity, roughness and grain sizes in the print layers just above the overhang compared with that obtained within the bulk alloy. These changes in microstructure compared with that obtained within the bulk alloy are likely to be associated with the excess heat generated during the laser processing of the overhang.
- A DOE was carried out to systematically ramp up the laser energy over up to 15 layers from the overhang to understand the effect of this localised overheating. This study demonstrated that lack of fusion pores were dominant when lower laser energy were used, while at higher laser powers, keyhole porosity was dominant. Overhang porosity ranged from 0.02 to 0.08%, while that within the bulk alloy was 0.02%. With lower energy laser processing conditions, increased porosity was also observed in the non-

overhang region of the print adjacent to the overhang due to ejection spatter from an 'unstable' overhang melt pool.

- The optimum processing conditions for the 2 x 10 mm overhang were associated with a gradual increase in the laser power and exposure time from the first overhang layer starting point of 47% of that used for the bulk alloy. The laser power and exposure time were then increased by 5% from the previous layer's values until the power returned to nominal levels after fifteen layers. This yielded a part with a relatively low overhang roughness and a porosity of 0.02%, similar to that of the bulk alloy.
- The in-situ process monitoring data from this study exhibited a strong correlation with the level of laser energy used to print each overhang layer and with the rate at which laser energy was ramped up to print each overhang layer. The overhang meltpool emission intensity was also found to correlate broadly with the porosity and roughness observed in the overhang structures. It was demonstrated that by utilizing printing conditions that minimized the level of overheating, particularly in the first three layers above the overhang, the level of porosity and roughness obtained was close to that observed for the bulk Ti-6Al-4V alloy.

5. Acknowledgements

This publication was produced from research supported in part by a research grant from Science Foundation Ireland (SFI) under Grant Number 16/RC/3872 and the SMART Eureka project APEM-AM. For the purpose of Open Access, the author has applied a CC by public copyright license to any Author Accepted Manuscript version arising from this submission. The authors would also like to acknowledge the support provided by the Stryker European Operations Limited.

References

[1] J. Li, R. Jin, and Z. Y. Hang, "Integration of physically-based and data-driven approaches for thermal field prediction in additive manufacturing," *Materials & Design,* vol. 139, pp. 473-485, 2018.

[2] L. E. Murr *et al.*, "Microstructure and mechanical behavior of Ti–6Al–4V produced by rapid-layer manufacturing, for biomedical applications," *Journal of the Mechanical Behavior of Biomedical Materials,* vol. 2, no. 1, pp. 20-32, 2009/01/01/ 2009, doi: https://doi.org/10.1016/j.jmbbm.2008.05.004.

[3] R. Liu, Z. Wang, T. Sparks, F. Liou, and J. Newkirk, "13 - Aerospace applications of laser additive manufacturing," in *Laser Additive Manufacturing*, M. Brandt Ed.: Woodhead Publishing, 2017, pp. 351-371.

[4] S. Clijsters, T. Craeghs, S. Buls, K. Kempen, and J.-P. Kruth, "In situ quality control of the selective laser melting process using a high-speed, real-time melt pool monitoring system," *The International Journal of Advanced Manufacturing Technology,* vol. 75, pp. 1089-1101, 2014.

[5] G. Kasperovich, J. Haubrich, J. Gussone, and G. Requena, "Correlation between porosity and processing parameters in TiAl6V4 produced by selective laser melting," *Materials & Design,* vol. 105, pp. 160-170, 2016.

[6] M. C. Sow *et al.*, "Influence of beam diameter on Laser Powder Bed Fusion (L-PBF) process," *Additive Manufacturing,* vol. 36, p. 101532, 2020/12/01/ 2020, doi: https://doi.org/10.1016/j.addma.2020.101532.

[7] H. Gong, K. Rafi, H. Gu, T. Starr, and B. Stucker, "Analysis of defect generation in Ti–6Al–4V parts made using powder bed fusion additive manufacturing processes," *Additive Manufacturing,* vol. 1, pp. 87-98, 2014.

[8] A. Sola and A. Nouri, "Microstructural porosity in additive manufacturing: The formation and detection of pores in metal parts fabricated by powder bed fusion," *Journal of Advanced Manufacturing and Processing,* vol. 1, no. 3, p. e10021, 2019.

[9] Z. Y. Chua, S. K. Moon, L. Jiao, and I. Ahn, "Geometric influence of the laser-based powder bed fusion process in Ti6AL4V and AlSi10Mg," *The International Journal of Advanced Manufacturing Technology,* vol. 114, no. 9, pp. 3165-3176, 2021.

[10] T. Craeghs, S. Clijsters, J. P. Kruth, F. Bechmann, and M. C. Ebert, "Detection of Process Failures in Layerwise Laser Melting with Optical Process Monitoring," *Physics Procedia,* vol. 39, pp. 753-759, 2012/01/01/ 2012, doi: https://doi.org/10.1016/j.phpro.2012.10.097.

[11] D. S. Egan, K. Jones, and D. P. Dowling, "Selective laser melting of Ti-6Al-4V: Comparing µCT with in-situ process monitoring data," *CIRP Journal of Manufacturing Science and Technology,* vol. 31, pp. 91-98, 2020/11/01/ 2020, doi: https://doi.org/10.1016/j.cirpj.2020.10.004.

[12] Q. Han, H. Gu, S. Soe, R. Setchi, F. Lacan, and J. Hill, "Manufacturability of AlSi10Mg overhang structures fabricated by laser powder bed fusion," *Materials & Design,* vol. 160, pp. 1080-1095, 2018/12/15/ 2018, doi: https://doi.org/10.1016/j.matdes.2018.10.043.

[13] L. Scime and J. Beuth, "Using machine learning to identify in-situ melt pool signatures indicative of flaw formation in a laser powder bed fusion additive manufacturing process," *Additive Manufacturing,* vol. 25, pp. 151-165, 2019/01/01/ 2019, doi: https://doi.org/10.1016/j.addma.2018.11.010.

[14] D. S. Egan and D. P. Dowling, "Correlating in-situ process monitoring data with the reduction in load bearing capacity of selective laser melted Ti–6Al–4V porous biomaterials," *Journal of the Mechanical Behavior of Biomedical Materials,* vol. 106, p. 103723, 2020.

[15] S. Rahmati and E. Vahabli, "Evaluation of analytical modeling for improvement of surface roughness of FDM test part using measurement results," *The International Journal of Advanced Manufacturing Technology,* vol. 79, no. 5, pp. 823-829, 2015.

[16] C. Qiu, C. Panwisawas, M. Ward, H. C. Basoalto, J. W. Brooks, and M. M. Attallah, "On the role of melt flow into the surface structure and porosity development during selective laser melting," *Acta Materialia,* vol. 96, pp. 72-79, 2015.

[17] J. Gockel, L. Sheridan, B. Koerper, and B. Whip, "The influence of additive manufacturing processing parameters on surface roughness and fatigue life," *International Journal of Fatigue,* vol. 124, pp. 380-388, 2019/07/01/ 2019, doi: https://doi.org/10.1016/j.ijfatigue.2019.03.025.

[18] D. Wang, Y. Yang, Z. Yi, and X. Su, "Research on the fabricating quality optimization of the overhanging surface in SLM process," *The International Journal of Advanced Manufacturing Technology,* vol. 65, no. 9, pp. 1471-1484, 2013.

[19] Y. Lee and W. Zhang, "Mesoscopic simulation of heat transfer and fluid flow in laser powder bed additive manufacturing," in *2015 International Solid Freeform Fabrication Symposium*, 2015: University of Texas at Austin.

[20] X. Xiao, C. Lu, Y. Fu, X. Ye, and L. Song, "Progress on experimental study of melt pool flow dynamics in laser material processing," in *Liquid Metals*: IntechOpen, 2021.

[21] R. Fabbro, K. Hirano, and S. Pang, "Analysis of the physical processes occurring during deep penetration laser welding under reduced pressure," *Journal of Laser Applications,* vol. 28, no. 2, p. 022427, 2016.

[22] Z. Wei and J. Du, "Heat and Mass Transfer of Additive Manufacturing Processes for Metals," in *Heat and Mass Transfer-Advances in Science and Technology Applications*: IntechOpen, 2019.

[23] C. S. Lough *et al.*, "Local prediction of Laser Powder Bed Fusion porosity by short-wave infrared imaging thermal feature porosity probability maps," *Journal of Materials Processing Technology,* vol. 302, p. 117473, 2022/04/01/ 2022, doi: https://doi.org/10.1016/j.jmatprotec.2021.117473.

[24] D. Alberts, D. Schwarze, and G. Witt, "In situ melt pool monitoring and the correlation to part density of Inconel® 718 for quality assurance in selective laser melting," in *2017 International Solid Freeform Fabrication Symposium*, 2017: University of Texas at Austin.

[25] S. Berumen, F. Bechmann, S. Lindner, J.-P. Kruth, and T. Craeghs, "Quality control of laser-and powder bed-based Additive Manufacturing (AM) technologies," *Physics procedia,* vol. 5, pp. 617-622, 2010.

[26] A. Gusarov and E. Kovalev, "Model of thermal conductivity in powder beds," *Physical Review B,* vol. 80, no. 2, p. 024202, 2009.

[27] T. DebRoy *et al.*, "Additive manufacturing of metallic components – Process, structure and properties," *Progress in Materials Science,* vol. 92, pp. 112-224, 2018/03/01/ 2018, doi: https://doi.org/10.1016/j.pmatsci.2017.10.001.

[28] M. J. Donachie, *Titanium: a technical guide*. ASM international, 2000.

[29] C. Cui, B. Hu, L. Zhao, and S. Liu, "Titanium alloy production technology, market prospects and industry development," *Materials & Design,* vol. 32, no. 3, pp. 1684-1691, 2011.

[30] S. Kelly and S. Kampe, "Microstructural evolution in laser-deposited multilayer Ti-6Al-4V builds: Part I. Microstructural characterization," *Metallurgical and Materials Transactions A,* vol. 35, no. 6, pp. 1861-1867, 2004.

[31] S. Cao, Y. Zou, C. V. S. Lim, and X. Wu, "Review of laser powder bed fusion (LPBF) fabricated Ti-6Al-4V: process, post-process treatment, microstructure, and property," *Light: Advanced Manufacturing,* vol. 2, no. 3, pp. 313-332, 2021.

[32] J. Li, X. Zhou, M. Brochu, N. Provatas, and Y. F. Zhao, "Solidification microstructure simulation of Ti-6Al-4V in metal additive manufacturing: A review," *Additive Manufacturing,* vol. 31, p. 100989, 2020/01/01/ 2020, doi: https://doi.org/10.1016/j.addma.2019.100989.

[33] F. R. Kaschel, M. Celikin, and D. P. Dowling, "Effects of laser power on geometry, microstructure and mechanical properties of printed Ti-6Al-4V parts," *Journal of Materials Processing Technology,* vol. 278, p. 116539, 2020/04/01/ 2020, doi: https://doi.org/10.1016/j.jmatprotec.2019.116539.

[34] S. Liu and Y. C. Shin, "Additive manufacturing of Ti6Al4V alloy: A review," *Materials & Design,* vol. 164, p. 107552, 2019/02/15/ 2019, doi: https://doi.org/10.1016/j.matdes.2018.107552.

[35] H. Galarraga, R. J. Warren, D. A. Lados, R. R. Dehoff, M. M. Kirka, and P. Nandwana, "Effects of heat treatments on microstructure and properties of Ti-6Al-4V ELI alloy fabricated by electron beam melting (EBM)," *Materials Science and Engineering: A,* vol. 685, pp. 417-428, 2017.

[36] F. Kaschel, R. Vijayaraghavan, P. J. McNally, D. P. Dowling, and M. Celikin, "In-situ XRD study on the effects of stress relaxation and phase transformation heat treatments on mechanical and microstructural behaviour of additively manufactured Ti-6Al-4V," *Materials Science and Engineering: A,* vol. 819, p. 141534, 2021.

[37] Renishaw-PLC. "Ti6Al4V ELI-0406 powder for additive manufacturing." Renishaw PLC. https://www.google.com/url?sa=t&rct=j&q=&esrc=s&source=web&cd=&ved=2ahUKEwjmgMfwx738AhURXcAKHe4yC4EQFnoECA8QAQ&url=https%3A%2F%2Fwww.renishaw.com%2Fmedia%2Fpdf%2Fen%2Fada9ffdf8ade44dbb9adb06ff5a74bbf.pdf&usg=AOvVaw0S_Vk-wSkxybSRHT8X58AV (accessed Jan 10th, 2023).

[38] Renishaw-PLC, "InfiniAM Spectral - Energy Input and Melt Pool Emissions Monitoring for AM Systems," 2017.

[39] G. Repossini, V. Laguzza, M. Grasso, and B. M. Colosimo, "On the use of spatter signature for in-situ monitoring of Laser Powder Bed Fusion," *Additive Manufacturing,* vol. 16, pp. 35-48, 2017.

[40] "Phoenix Nanotom M 180 kV / 20 W X-ray nanoCT® system for high-resolution analysis and 3D metrology," ed. Cincinnati, Ohio, 2021.

[41] VGStudio, "VGStudio Max 2.2 Reference Manual," ed. Heidelberg, Germany: VGStudio, 2012.

[42] G. Kerckhofs, G. Pyka, M. Moesen, J. Schrooten, and M. Wevers, "High-resolution micro-CT as a tool for 3D surface roughness measurement of 3D additive manufactured porous structures," in *Proc iCT*, 2012, pp. 77-83.
[43] D. Arola and M. Ramulu, "An examination of the effects from surface texture on the strength of fiber reinforced plastics," *Journal of Composite materials,* vol. 33, no. 2, pp. 102-123, 1999.
[44] D. Greitemeier, C. Dalle Donne, F. Syassen, J. Eufinger, and T. Melz, "Effect of surface roughness on fatigue performance of additive manufactured Ti–6Al–4V," *Materials Science and Technology,* vol. 32, no. 7, pp. 629-634, 2016.
[45] B. Taylor and E. Weidmann. "Metallographic preparation of titanium." Struers. https://www.struers.com/-/media/Struers-media-library/Materials/Application-reports/Application_Note_Titanium_2015_ENG.pdf (accessed 27/07, 2022).
[46] B. Vrancken, L. Thijs, J.-P. Kruth, and J. Van Humbeeck, "Heat treatment of Ti6Al4V produced by Selective Laser Melting: Microstructure and mechanical properties," *Journal of Alloys and Compounds,* vol. 541, pp. 177-185, 2012/11/15/ 2012, doi: https://doi.org/10.1016/j.jallcom.2012.07.022.
[47] F. Kaschel, M. Celikin, and D. P. Dowling, "Effects of laser power on geometry, microstructure and mechanical properties of printed Ti-6Al-4V parts," *Journal of Materials Processing Technology,* vol. 278, p. 116539, 2020.
[48] A. Gornakova and S. Prokofjev, "Energetics of intergranular and interphase boundaries in Ti–6Al–4V alloy," *Journal of Materials Science,* vol. 55, pp. 9225-9236, 2020.
[49] S. Lee, J. Kim, J. Choe, S.-W. Kim, J.-K. Hong, and Y. S. Choi, "Understanding crack formation mechanisms of Ti–48Al–2Cr–2Nb single tracks during laser powder bed fusion," *Metals and Materials International,* vol. 27, pp. 78-91, 2021.
[50] M. Tang, P. C. Pistorius, and J. L. Beuth, "Prediction of lack-of-fusion porosity for powder bed fusion," *Additive Manufacturing,* vol. 14, pp. 39-48, 2017/03/01/ 2017, doi: https://doi.org/10.1016/j.addma.2016.12.001.
[51] S. Shrestha and K. Chou, "Formation of keyhole and lack of fusion pores during the laser powder bed fusion process," *Manufacturing Letters,* vol. 32, pp. 19-23, 2022.
[52] S. Keaveney, A. Shmeliov, V. Nicolosi, and D. P. Dowling, "Investigation of process by-products during the Selective Laser Melting of Ti6AL4V powder," *Additive Manufacturing,* vol. 36, p. 101514, 2020/12/01/ 2020, doi: https://doi.org/10.1016/j.addma.2020.101514.
[53] J. C. Fox, S. P. Moylan, and B. M. Lane, "Effect of Process Parameters on the Surface Roughness of Overhanging Structures in Laser Powder Bed Fusion Additive Manufacturing," *Procedia CIRP,* vol. 45, pp. 131-134, 2016/01/01/ 2016, doi: https://doi.org/10.1016/j.procir.2016.02.347.